FeSe$_2$-Decorated Bi$_2$Se$_3$ Nanosheets Fabricated via Cation Exchange for Chelator-Free ^{64}Cu-labeling and Multimodal Image-Guided Photothermal-Radiation Therapy

Dr. Liang Cheng,
Institute of Functional Nano & Soft Materials Laboratory (FUNSOM), Collaborative Innovation Center of Suzhou Nano Science and Technology, Soochow University, Suzhou, Jiangsu 215123, China

Mr. Sida Shen,
Institute of Functional Nano & Soft Materials Laboratory (FUNSOM), Collaborative Innovation Center of Suzhou Nano Science and Technology, Soochow University, Suzhou, Jiangsu 215123, China

Mr. Sixiang Shi,
Materials Science Program, University of Wisconsin–Madison, Madison, Wisconsin, United States

Mr. Yuan Yi,
School of Radiation Medicine and Protection & School for Radiological and Interdisciplinary Sciences (RAD-X), Jiangsu Provincial Key Laboratory of Radiation Medicine and Protection, Soochow University, Suzhou, Jiangsu 215123, China

Mr. Xiaoyong Wang,
Center for Molecular Imaging and Translational Medicine, School of Public Health, Xiamen University, Xiamen, Fujian 361005, China

Dr. Guosheng Song,
Institute of Functional Nano & Soft Materials Laboratory (FUNSOM), Collaborative Innovation Center of Suzhou Nano Science and Technology, Soochow University, Suzhou, Jiangsu 215123, China

Dr. Kai Yang,
School of Radiation Medicine and Protection & School for Radiological and Interdisciplinary Sciences (RAD-X), Jiangsu Provincial Key Laboratory of Radiation Medicine and Protection, Soochow University, Suzhou, Jiangsu 215123, China

Dr. Gang Liu,
Center for Molecular Imaging and Translational Medicine, School of Public Health, Xiamen University, Xiamen, Fujian 361005, China

Correspondence to: Liang Cheng, lcheng2@suda.edu.cn; Weibo Cai, wcai@uwhealth.org; Zhuang Liu, zliu@suda.edu.cn.

Prof. Todd E. Barnhart,

Department of Medical Physics, University of Wisconsin–Madison, Madison, Wisconsin, United States

Prof. Weibo Cai, and

Department of Radiology, University of Wisconsin–Madison, Madison, Wisconsin, United States

Prof. Zhuang Liu

Institute of Functional Nano & Soft Materials Laboratory (FUNSOM), Collaborative Innovation Center of Suzhou Nano Science and Technology, Soochow University, Suzhou, Jiangsu 215123, China

Liang Cheng: lcheng2@suda.edu.cn; Weibo Cai: wcai@uwhealth.org; Zhuang Liu: zliu@suda.edu.cn

Abstract

Multifunctional theranostic agents have become rather attractive to realize image-guided combination cancer therapy. Herein, we develop a novel method to synthesize Bi_2Se_3 nanosheets decorated with mono-dispersed $FeSe_2$ nanoparticles ($FeSe_2/Bi_2Se_3$) for tetra-modal image-guided combined photothermal & radiation tumor therapy. Interestingly, upon addition of $Bi(NO_3)_3$, pre-made $FeSe_2$ nanoparticles via cation exchange would be gradually converted into Bi_2Se_3 nanosheets, on which remaining $FeSe_2$ nanoparticles are decorated. The yielded $FeSe_2/Bi_2Se_3$ composite-nanostructures were then modified with polyethylene glycol (PEG). Taking advantages of the high r_2 relaxivity of $FeSe_2$, the X-ray attenuation ability of Bi_2Se_3, the strong near-infrared (NIR) optical absorbance of the whole nanostructure, as well as the chelate-free radiolabeling of ^{64}Cu on $FeSe_2/Bi_2Se_3$-PEG, *in vivo* magnetic resonance (MR)/computer tomography (CT)/photoacoustic (PA)/position emission tomography (PET) multimodal imaging was carried out, revealing efficient tumor homing of $FeSe_2/Bi_2Se_3$-PEG after intravenous injection. Utilizing the intrinsic physical properties of $FeSe_2/Bi_2Se_3$-PEG, *in vivo* photothermal & radiation therapy to achieve synergistic tumor destruction was then realized, without causing obvious toxicity to the treated animals. Our work presents a unique method to synthesize composite-nanostructures with highly integrated functionalities, promising not only for nano-biomedicine, but also potentially for other different nanotechnology fields.

Keywords

$FeSe_2/Bi_2Se_3$ nanostructures; Cation exchange; Chelator-free radiolabeling; Multimodal imaging; Photothermal-radiation therapy treatment

1. Introduction

With the development of material science and nanotechnology, multifunctional nanomaterials have attracted ever-increasing attention in nanomedicine, especially in cancer theranostics[1]. On one hand, the integration of several different imaging functions into a single nano-platform would facilitate multimodal imaging and overcome the limitations of each single imaging modality, so as to achieve more precise diagnosis/prognosis of diseases such as cancer[2]. On the other hand, many multifunctional nanomaterials are also useful in cancer treatment, either serving as drug carriers by loading with therapeutic agents, or

destructing tumors with their inherent properties usually under external physical stimuli[3]. For the latter case, nanoparticles containing high-Z elements (e.g. Au[4], I, Bi[5], and rare earth elements[6]) which are able to interact with and absorb ionizing radiation could be utilized to enhance the efficacy of radiation therapy (RT)[7], while those with high optical absorbance in the near infrared (NIR) region may convert photon energy into heat to induce photothermal therapy (PTT) of tumors[1d, 8]. The combination of different therapeutic strategies using multifunctional nanomedicine may offer synergistic effects in cancer treatment, so as to effectively treat tumors with decreased therapeutic doses and thus reduced side effects [9]. Moreover, to optimize the therapeutic planning and monitor treatment responses, image-guided therapies have also been developed as a new concept to achieve highly efficient and accurate treatments of cancers[2c, 8j, 10]. Therefore, to this end, there is still much need to construct multifunctional nanostructures via simplified and reliable methods for multimodal image-guided combination tumor therapy.

Bismuth (Bi)-based nanoparticles are one of the promising candidates not only as contrast agents for X-ray computed tomography (CT) imaging, but also as sensitizing agents to enhance the efficacy of RT cancer treatment, due to the high photoelectric absorption coefficient[11], which is significantly higher than that of the well-known gold-based radiation sensitizers. A number of reports have also uncovered that Bi-containing nanostructures, such as Bi_2Se_3 nanoplates protected by poly (vinylpyrollidone), showed low in vivo toxicity and could be gradually cleared from the body overtime[12]. Therefore, it would be interesting to develop Bi-based nanostructures integrated with other functional nano-components, so that we may realize different imaging and therapeutic functions via a synergistic manner using one single agent.

In this work, we develop a unique yet simple method to construct a new type of two-dimensional Bi_2Se_3 nanosheets integrated with magnetic sub-nanostructures for multimodal imaging and combination cancer therapy (Scheme 1). It is found that pre-made $FeSe_2$ nanoparticles upon addition of $Bi(NO_3)_3$ under a high temperature would be gradually converted into Bi_2Se_3 nanosheets via cation exchange, obtaining $FeSe_2$ decorated Bi_2Se_3 ($FeSe_2/Bi_2S_3$) which is further modified with polyethylene glycol (PEG). Utilizing the intriguing physical properties of such composite nanostructure, as well as by labeling $FeSe_2/Bi_2Se_3$-PEG with radioisotope ^{64}Cu via a chelate-free method, in vivo CT, magnetic resonance (MR), photoacoustic (PA), and positron emission tomography (PET) tetra-modal imaging is conducted for tumor-bearing mice. The observed efficient tumor accumulation of $FeSe_2/Bi_2S_3$-PEG allows us to further use this agent for combined PTT and RT treatments, which are based on the NIR absorbance and X-ray attenuation abilities of such nanostructure, respectively. A remarkable synergistic tumor destruction effect is achieved after intravenous (i.v.) injection of $FeSe_2/Bi_2Se_3$-PEG and the followed NIR laser & X-ray irradiation. Finally, systematic in vivo toxicology evaluation uncovers no appreciable toxicity of our $FeSe_2/Bi_2S_3$-PEG to the treated mice over 30 days. Our work here presents a facile cation exchange method to incorporate multiple functionalities into a single Bi-based nanoplatform, which shows great promises in cancer theranostics.

2. Results and Discussion

Bi_2Se_3 nanosheets decorated with $FeSe_2$ nanoparticles ($FeSe_2/Bi_2Se_3$) were synthesized in a mixed solvent of oleyamine (OM) and 1-octadecene (ODE) under N_2 atmosphere via a one-step cation exchange method. Firstly, uniform ultra-small $FeSe_2$ nanoparticles were synthesized after injection of Se/OM into $FeCl_2$ dissolved in OM/ODE mixed solvent at 150 °C. As-synthesized $FeSe_2$ nanoparticles showed uniform sizes with an average diameter of ~ 8 nm as observed under transmission electron microscope (TEM) (Figure 1A). X-ray diffraction (XRD) spectrum further confirmed the orthorhombic ferroselite structure of as-synthesized $FeSe_2$ nanoparticles (Supporting Figure S1). Afterwards, $Bi(NO_3)_3$ dissolved in diethylene glycol (DEG) was injected into the above mixture and reacted for another 30 min at 150°C. Interestingly, in the final product, we observed small $FeSe_2$ nanoparticles uniformly decorated on newly formed nanosheets, which had average size and thickness of ~100 nm and ~ 2.6 nm, respectively, as revealed by both TEM imaging and atomic force microscopy imaging (Figure 1B, Supporting Figure S2). X-ray diffraction (XRD) analysis was also performed to further investigate the structural information of the whole nanostructures. As showed in Figure 1C, the representative diffraction peaks matched well with the standard pattern of $FeSe_2$ (JCPDS card No. 21-0432) and Bi_2Se_3 (JCPDS card No. 33-0214), suggesting the co-existence of $FeSe_2$ and Bi_2Se_3 nanostructures in the obtained nano-composite. Under high-resolution TEM (HR-TEM) imaging (Figure 1B, **inset**), we observed clear lattice spacing at 0.305 nm and 0.26 nm, which should belong to the (1, 1, 1) plane of $FeSe_2$ and the (0, 0, 6) plane of Bi_2Se_3, respectively. High-angle annular dark field scanning transmission electron microscopy (HADDF-STEM-EDS) elemental mapping also confirmed that $FeSe_2$ nanoparticles were decorated on the newly generated Bi_2Se_3 nanosheets (Figure 1D, Supporting Figure S3). Moreover, in the X-ray photoelectron spectroscopy (XPS) spectra of the obtained composite-nanostructure (Supporting Figure S4), characteristic peaks of Bi, Fe, and Se were observed.

To understand the mechanism of how $FeSe_2$ nanoparticles are transformed into $FeSe_2/Bi_2Se_3$ particle-sheet composite-nanostructures, we carefully studied how the synthesis parameters would affect the formation of nanocomposites. Interestingly, we found that the density of $FeSe_2$ nanoparticles decorated on the surface of the Bi_2Se_3 nanosheets could be tuned by changing the amount of added $Bi(NO_3)_3$ (Figure 2A, Supporting Figure S5). With a small amount of Bi^{3+} added (at the Bi : Fe ratio of 0.2 : 1), Bi_2Se_3 nanosheets were immediately formed with $FeSe_2$ nanoparticles decorated on their surface. As the further increase of added Bi^{3+}, the density of $FeSe_2$ nanoparticles on the formed nanosheets reduced. Notably, if excess Bi^{3+} was added, all $FeSe_2$ nanoparticles were completely disappeared, with only large Bi_2Se_3 nanosheets left. In the meanwhile, prolonging of reaction time would also be favorable for the conversion of $FeSe_2$ nanoparticles into Bi_2Se_3 nanosheets. XRD spectra were also used to monitor the whole process (Figure 2B). It could be found that the intensities of $FeSe_2$ nanoparticles decreased only by a little with small amounts of Bi^{3+} were added (at the Bi : Fe ratios of 0.2 : 1 and 0.5 : 1) (Supporting Figure S6a&6b). However, the $FeSe_2$-characterstic peaks became rather weak at the Bi : Fe ratio of 1.5 : 1, and completely disappeared at the Bi : Fe ratio of 2 : 1, after reaction for 30 min at 150 °C (Supporting Figure S6c&6d), consistent with the TEM results. The exact Bi : Fe

ratios in the $FeSe_2/Bi_2Se_3$ composite-nanostructures were measured to be 0.21 : 1, 0.4 : 1, 0.95 : 1, 4.1 : 1, and 24 : 1 prepared with the feeding Fe to Bi ratios at 0.2 : 1, 0.5 : 1, 1 : 1, 1.5 : 1 and 2 : 1, respectively, for products obtained after 0.5 h of reaction (Figure 2C). In our followed experiments, we chose $FeSe_2/Bi_2Se_3$ prepared at the feeding Bi: Fe ratio of 1 : 1 (30 min of reaction time) for further studies.

Based on the above experimental results, we proposed a mechanism for the growth of $FeSe_2/Bi_2Se_3$ nanostructures as follows (Figure 2D). Firstly, when uniform $FeSe_2$ nanoparticles are synthesized, excessive Se remains existed in the system after the reaction. After Bi^{3+} is added into this system, Bi_2Se_3 nanosheets are formed immediately due to excessive Se. However, after more Bi^{3+} is introduced into the reaction system, free Se would be completely consumed. After that point, those pre-made $FeSe_2$ nanoparticles could act at a Se donor to allow the formation of Bi_2Se_3 nanosheets, owing to the fact that the bond dissociation energy (BDE) of Fe-Se (BDE < 239 ± 9.2) is much lower than that of Bi-Se (BDE = 280.3 ± 5.9)[13]. Such cation exchange of Fe^{2+} by Bi^{3+} in their respective selenides occurs on the interface between $FeSe_2$ and Bi_2Se_3, therefore these two components are attached together in formed composite-nanostructure. Further increase of added Bi^{3+} would lead to the complete dissolution of $FeSe_2$ nanoparticles, leaving pure Bi_2Se_3 nanosheets with large sizes in the final product. Cation exchange reaction has emerged as a new strategy for the fabrication of nanomaterials via post-synthetic chemical modification. The cations of a pre-synthesized nanocrystal can be partially or completely replaced by new guest cations, often with preservation of its size, shape, and, in some cases, even crystal structure[14]. The observed morphology change of $FeSe_2/Bi_2Se_3$ nanostructure after cation exchange may be accounted for the changes in the crystal unit cell symmetry and lattice parameters of $FeSe_2$ and Bi_2Se_3 during the transformation, just like the transformation of CdSe nanorods into Ag_2Se nanostructures with different morphologies [14b]. We also hypothesize that since $FeSe_2$ and Bi_2Se_3 have quite different crystalline structures, $FeSe_2$ nanoparticles would be on the surface of Bi_2Se_3 nanosheets instead of doping in the nanosheets.

Next, we functionalize as-made $FeSe_2/Bi_2Se_3$ with a PEG-grafted amphiphilic polymer. After PEGylation, the obtained $FeSe_2/Bi_2Se_3$-PEG with an average hydrodynamic size at ~140 nm exhibited great stability in various physiological solutions including saline, cell medium, and serum (Figure 3A, **inset**, Supporting Figure S7). Moreover, with such biocompatible PEG coating, our $FeSe_2/Bi_2Se_3$-PEG showed no significant *in vitro* cytotoxicity to cells even under high nanostructure concentrations (Supporting Figure S8).

The physical properties of $FeSe_2/Bi_2Se_3$-PEG were then studied in detail. High optical absorbance in a wide spectrum range from 700~1000 nm was observed for $FeSe_2/Bi_2Se_3$-PEG (Figure 3A). The mass extinction co-efficient of $FeSe_2/Bi_2Se_3$-PEG at 800 nm was measured to be 34.5 $Lg^{-1}cm^{-1}$, which was much higher than that of graphene oxide (GO, 3.6 $Lg^{-1}cm^{-1}$)[15], reduced graphene oxide (21.1 L $g^{-1}cm^{-1}$)[8a], MoS_2 nanosheets (29.2 L $g^{-1}cm^{-1}$)[16], and WS_2 nanosheets (23.8 L $g^{-1}cm^{-1}$)[8i]. As expected, owing to its high NIR absorbance, $FeSe_2/Bi_2Se_3$-PEG showed a strong photothermal conversion efficiency and could be effectively heated up under exposure to an 808-nm NIR laser (Figure 3B, Supporting Figure S9). After laser irradiation for half an hour, we did not find any obvious

decay in its NIR absorbance, indicating the high photo-stability of such $FeSe_2/Bi_2Se_3$-PEG agent (Supporting Figure S10).

As far as the magnetic property of such composite-nanostructure is concerned, the absence of a hysteresis loop in the field-dependent magnetization measurement illustrated the superparamagnetic nature of $FeSe_2/Bi_2Se_3$-PEG[17] (Supporting Figure S11). T2-weighted MR images of a series of concentrations of $FeSe_2/Bi_2Se_3$-PEG solutions acquired by a 3T MR scanner revealed the concentration-dependent darkening effect (Figure 3C). The transverse relaxivity (r2) of $FeSe_2/Bi_2Se_3$-PEG was calculated to be 136.68 $mM^{-1}S^{-1}$ (Figure 3D), which was higher than that of Fe_3O_4 (99.6 $mM^{-1}S^{-1}$), and other Fe-based clinical contrast agents (72 $mM^{-1}S^{-1}$ for Ferumoxsil, 151 $mM^{-1}S^{-1}$ for Ferrixan, and 98.3 $mM^{-1}S^{-1}$ for Ferumoxide)[18], promising the use of $FeSe_2/Bi_2Se_3$-PEG as a T2-MR contrast agent.

On the other hand, since Bismuth (Bi) processes larger X-ray absorption coefficient than that of other reported and extensively applied elements (Bi : 5.74, Au : 5.16, W : 4.44, and I : 1.94 cm^{-2} kg^{-1} at 100 keV)[19], it is expected that $FeSe_2/Bi_2Se_3$-PEG could also provide strong contrast under CT imaging. With increasing nanostructure concentrations, the CT signals of $FeSe_2/Bi_2Se_3$-PEG solutions were enhanced (Figure 3E). Meanwhile, the Hounsfield Unit (HU) values of $FeSe_2/Bi_2Se_3$-PEG followed a good linear relation with Bi concentrations (Figure 3F). Therefore, the inherent physical properties of $FeSe_2/Bi_2Se_3$-PEG are promising to offer contrasts under a variety of imaging modalities.

Next, we would like use $FeSe_2/Bi_2Se_3$-PEG as a multiple imaging contrast agent by taking advantages of its abovementioned physical properties. Magnetic resonance (MR) imaging can provide excellent soft-tissue morphological details together with functional information on lesions with high spatial resolution[2b, 20]. Mice bearing 4T1 tumors were *i.v.* injected with $FeSe_2/Bi_2Se_3$-PEG (dose=20 mg/kg) and imaged by 3T clinical MR scanner equipped with a small animal imaging coil. Remarkable darkening effect in the tumor of injected mice was observed after 24 h (Figure 4A&4C), suggesting the high passive tumor uptake of $FeSe_2/Bi_2Se_3$-PEG likely via the enhanced permeability and retention (EPR) effect of cancerous tumors.

X-ray computed tomography (CT) is featured with the advantages of high resolution, no depth limitation, and the capability for three-dimensional (3D) reconstruction[21]. Then the *in vivo* CT imaging was conducted by administrating $FeSe_2/Bi_2Se_3$-PEG via *i.v.* injection route into 4T1 tumor-bearing mice. As showed in Figure 4B, it was found that the HU values in the liver and tumor increased obviously after $FeSe_2/Bi_2Se_3$-PEG injection (Figure 4C), consistent to the MR imaging results.

Photoacoustic imaging (PA), which is a relatively new biomedical imaging modality developed based on the photoacoustic effect of light-absorbers, offers remarkably increased imaging depth and spatial resolution compared to traditional *in vivo* optical imaging[22]. With strong NIR absorbance, $FeSe_2/Bi_2Se_3$-PEG could also serve as a contrast agent for *in vivo* PA imaging. Mice bearing 4T1 tumors were *i.v.* injected with $FeSe_2/Bi_2Se_3$-PEG (2 mg/mL, 200 μL) and imaged under a PA imaging system (excitation wavelength = 800 nm).

As shown in Figure 4D&4E, the initial PA signal in the tumor site before injection was rather weak. After injection of $FeSe_2/Bi_2Se_3$-PEG nanostructures, the PA signal in tumor tissue became stronger over time due to the passive tumor accumulation of nanoparticles. The whole tumor was brightened up later on, indicating that a large amount of $FeSe_2/Bi_2Se_3$-PEG nanoparticles were homogenously accumulated inside the tumor.

Nuclear imaging techniques such as PET offers great imaging sensitivity incomparable by other imaging modalities, and have been extensively used as a molecular imaging tool for disease diagnosis and prognosis [23]. The majority of biomolecules or nanoparticles are labeled with isotopes with the help of chelator molecules such as 1,4,7-triazacyclononane-1,4,7-triaceti acid (NOTA) or 1,4,7,10-tetraazacyclododecane-1,4,7,10-tetraacetic acid (DOTA)[24]. Reliable chelator-free radiolabeling techniques have recently emerged as a promising alternative approach to label nanoparticles in a simple way[25]. Considering the high affinity between copper and chalcogen atoms[26], we thus hypothesized that our $FeSe_2/Bi_2Se_3$ might be labeled with ^{64}Cu via a chelator-free approach.

In our experiments, ^{64}Cu labeling was straightforwardly executed by mixing $^{64}CuCl_2$ with $FeSe_2/Bi_2Se_3$-PEG at 37°C for 1h under constant shaking (Figure 5A). We found that ^{64}Cu was immediately adsorbed by $FeSe_2/Bi_2Se_3$-PEG as detected by thin-layer chromatography (TLC), with the labeling yield measured to be as high as 95% after 1 h of incubation (Figure 5B, Supporting Figure S12). Moreover, the ^{64}Cu labeling in ^{64}Cu-$FeSe_2/Bi_2Se_3$-PEG was also found to be relatively stable in serum within 24 h (Figure 5C), with ~ 16 % of ^{64}Cu released from the system. Such a highly efficient and stable chelator-free labeling method is possibly due to the anchoring of Cu^{2+} on the Bi defect sites of on the $FeSe_2/Bi_2Se_3$ nanostructures. PET scans of 4T1 tumor-bearing mice were then performed using a microPET Inveon rodent model scanner at various time points post *i.v.* injection of ^{64}Cu-$FeSe_2/Bi_2Se_3$-PEG (5~10 MBq). Obvious tumor contrast was observed after injection of ^{64}Cu-$FeSe_2/Bi_2Se_3$-PEG, and reached to a rather high level in 6 hours, suggesting efficient tumor retention of those nanostructures due to the EPR effect of cancerous tumors (Figure 5D&5E), in good agreement with the previous MR/CT/PA imaging results (Supporting Figure S13) and microscope images of Prussian blue stained tumor slices (iron staining, Supporting Figure S14).

From the above results, our synthesized $FeSe_2/Bi_2Se_3$-PEG could be successfully used as a MR/CT/PA/PET tetra-modal imaging contrast agent. Each imaging modality has its own unique advantages along with intrinsic limitations. For example, MRI/CT imaging have their disadvantages such as relatively low sensitivity, while PA imaging has limited depth penetration. PET imaging, although sensitive enough, is not able to provide anatomy information during imaging[2a]. To solve this problem, multimodal imaging is a powerful method that can provide more reliable and accurate detection of diseased sites. While MR and CT imaging techniques offer 3D images with anatomic information, PET imaging would be able to qualify the tumor retention of nano-agents in real-time. In the meanwhile, PA imaging with high spatial resolution may be used to investigate the detailed intratumoral distribution of nanoparticles, useful for the better prediction/understanding of therapeutic effects. Therefore, the combination of those different imaging modalities would be of great importance to provide valuable information for better therapeutic planning.

Considering the strong NIR absorbance of $FeSe_2/Bi_2Se_3$, we next tested the *in vitro* photothermal performance of $FeSe_2/Bi_2Se_3$-PEG under NIR laser exposure. 4T1 cells were incubated with different concentrations of $FeSe_2/Bi_2Se_3$-PEG for 6 h and then irradiated by the 808-nm laser for 5 min at the power density of 0.8 W/cm^2. Cell viability assay was conducted to determine the cancer cell killing efficiency of PTT at different concentrations of $FeSe_2/Bi_2Se_3$-PEG (Figure 6A). As expected, enhanced cancer cell ablation was observed as the increase of nanoparticle concentrations. Confocal fluorescent images of Calcine AM and propidium iodide (PI) co-stained cells further confirmed the effective and specific photothermal ablation of 4T1 cells induced by $FeSe_2/Bi_2Se_3$-PEG (Figure 6B), demonstrating that our $FeSe_2/Bi_2Se_3$-PEG could be used as an effective PTT agent.

Next, we wondered whether $FeSe_2/Bi_2Se_3$-PEG with strong X-ray attenuation ability would be able to enhance radiotherapy triggered by ionizing radiation such as X-ray. A sequence variant of histone H2A called H2AX is one of the key components of chromatin involved in DNA damage response induced by different genotoxic stresses. Phosphorylated H2AX (γ-H2AX) would be rapidly concentrated in chromatin domains around DNA double-strand breaks (DSBs) after the action of ionizing radiation or chemical agents. γ-H2AX foci could be easily detected in cell nuclei using immunofluorescence microscopy that allowed to use γ-H2AX as a quantitative marker of DSBs in various applications [27]. Immunofluorescent images, as showed in Figure 6C, revealed low levels of γ-H2AX fluorescent spots in PBS treated after X-ray irradiation, as well as cells incubated with $FeSe_2/Bi_2Se_3$-PEG in the absence of X-ray irradiation. In contrast, the cells irradiated in the presence of $FeSe_2/Bi_2Se_3$-PEG exhibited a noticeably higher density of γ-H2AX foci, indicating higher number of DNA double-strand breaks. Furthermore, the clonogenic survival assay (Figure 6D, Supporting Figure S15) demonstrated a decrease of viable cell colonies after treatment with $FeSe_2/Bi_2Se_3$-PEG and X-ray irradiation, compared to those receiving irradiation alone. The radiation enhancement is regarded to be the photoelectric effect and Compton scattering of Bi from $FeSe_2/Bi_2Se_3$-PEG[28], which once engulfed by tumor cells could absorb and concentrate the radiation dose to enhance the radiation-induced cell damage.

Considering the capability of $FeSe_2/Bi_2Se_3$-PEG to induce *in vitro* PTT and enhance *in vitro* RT, as well as the effective *in vivo* tumor retention of those nanoparticles by the EPR effect, we then would like to use $FeSe_2/Bi_2Se_3$-PEG for *in vivo* cancer treatment, aiming at the synergistic therapeutic outcome with PTT and RT combined together. According to the above PET/PA/MRI/CT tetra-modal imaging results, we conducted PTT and RT at 24 h p.i., at which time point nanoparticles showed the highest tumor accumulation, in order to achieve the optimized therapeutic outcomes. After being *i.v.* injected with $FeSe_2/Bi_2Se_3$-PEG for 24 h (2 mg/mL, 200 μL for each mouse), mice bearing 4T1 tumors were anesthetized and exposed to the 808-nm laser at the power density of 0.5 W/cm^2. An infrared (IR) thermal mapping apparatus was used to record the temperature change in the tumor area under NIR irradiation. From mice *i.v.* injected with $FeSe_2/Bi_2Se_3$-PEG, their tumors surface temperature rapidly increased from ~28 °C to ~46 °C within 1 min of laser irradiation and kept at this temperature for 10 min (Figure 7A&B). In comparison, the tumors on mice with PBS injection under the same irradiation condition showed no significant heating effect.

Next, the *in vivo* cancer treatment efficacy of combination therapy induced by $FeSe_2/Bi_2Se_3$-PEG was evaluated. Mice bearing 4T1 tumors (volume ~70 mm^3) were randomly divided into seven groups (n= 5 per group): (i) untreated control, (ii) Laser only, (iii) *i.v.* injected with $FeSe_2/Bi_2Se_3$-PEG, (iv) *i.v.* injected with $FeSe_2/Bi_2Se_3$-PEG + NIR, (v) RT only, (vi) *i.v.* injected with $FeSe_2/Bi_2Se_3$-PEG +RT, (vii) *i.v.* injected with $FeSe_2/Bi_2Se_3$-PEG+NIR+RT. The doses of $FeSe_2/Bi_2Se_3$-PEG were fixed at 20 mg/kg in the above groups. PTT was introduced by 808-nm light irradiation with a power density of 0.5 W/cm^2 for 10 min, while the X-ray radiation dose for RT was fixed at 4 Gy. As expected, i.v. injection of $FeSe_2/Bi_2Se_3$-PEG with mild photothermal heating showed no appreciable effect to the tumor growth (group iv) (Figure 7C). The efficacy of RT with X-ray irradiation of tumors, although could be partly enhanced by i.v. injection with $FeSe_2/Bi_2Se_3$-PEG, was still not satisfactory (group vi and vii). In marked contrast, tumors on mice after $FeSe_2/Bi_2Se_3$-PEG injected and combined PTT+RT showed significantly delayed tumor growth (group vii), demonstrating the obvious advantage and synergistic effect of the combined RT & PTT in comparison to mono-therapies (Supporting Figure S16).

The anti-tumor efficacies of different treatments were further assessed by hexatoxylin and eosin H&E staining (Figure 7D). While the tumors in $FeSe_2/Bi_2Se_3$-PEG treated mice were only partially destroyed after irradiating with either NIR laser (group iv) or X-ray (group vi), for the combination therapy with $FeSe_2/Bi_2Se_3$-PEG + X-ray + NIR treatment, the tumor cells were severely destructed, as indicated by more vacuoles, condensed nuclei, and changed cell shapes found in this group. The synergistic therapeutic effects of the combined PTT&RT may be attributed to be as follows: The Bi atoms in the $FeSe_2/Bi_2Se_3$ nanostructures possess a strong photoelectric absorbance capacity, and are able to generate numerous short-range secondary electrons under X-ray radiation to accelerate the DNA breaking. On the other hand, under the mild photothermal triggered by $FeSe_2/Bi_2Se_3$-PEG, the overall tumor oxygenation status could be improved, thus leading to a radiation enhancement effect during RT[29].

Investigation of toxicity and clearance of new materials is important for possible medical applications. To investigate whether $FeSe_2/Bi_2Se_3$-PEG would result in any side effect, we then conducted a series of experiment *in vivo*, including the biodistribution and blood biochemistry analysis. Healthy mice (5 per group) *i.v.* injected of $FeSe_2/Bi_2Se_3$-PEG (2 mg/mL, 200 μL), were scarified at the 7th, 14th, and 30th day, with their main organs harvested for biodistribution study, which was based on ICP-AES measurement of Bi levels in solubilized organs (Figure 8A). The Bi levels were found to be as high as 15.5 ± 2.7 % of the injected dose per gram tissue (%ID/g) in the liver, 36.4 ± 8.7 %ID/g in the spleen, and 0.9 ± 0.3 %ID/g in the kidney at 7 days post injection (p.i.). After 30 day, the Bi levels decreased to 2.3 ±1.5 %ID/g in the liver, 5.9 ± 2.6 %ID/g in the spleen, and 0.6 ± 0.4% ID/g in the kidney. Such time-dependent clearance is similar to findings in a previous work reporting that Bi_2Se_3 nanoplates protected by poly (vinylpyrollidone) could be gradually metabolized by the liver and get excreted from the body overtime[12a]. Prussia blue staining of spleen slices also evidenced the gradual clearance of Fe element from mice *i.v.* injected with $FeSe_2/Bi_2Se_3$-PEG (Figure 8B). It is proposed that nanoparticles less than 5~6 nm can be quickly cleared through the kidney while large-sized nanoparticles above 50 nm maybe undergo a much slower excretion by the liver via the bile duct into feces[30]. It is possible

that $FeSe_2/Bi_2Se_3$ nanostructures after being engulfed by Kupffer cells in RES organs may be gradually decomposed into small complexes to facilitate such relatively rapid excretion, which is obviously favorable to eliminate potential long-term toxicities.

Next, we performed the standard biochemistry examination with the mice treated by the $FeSe_2/Bi_2Se_3$-PEG at the different time points. The serum biochemical parameters including alanine transaminase (ALT), aspartate transaminase (AST), and blood urea nitrogen (BUN), as well as standard hematology markers, were both tested (Figure 8C&8D, Supporting Table S1). During the whole treatment, we did not find any toxicity to the mice after injection $FeSe_2/Bi_2Se_3$-PEG. Finally, we collected liver, spleen, kidney, heart, and lung for H&E staining (Supporting Figure S17). No significant organ damage was observed in those organs from mice treated with $FeSe_2/Bi_2Se_3$-PEG within 30 days. Considering the very little retention of Bi and Fe after 30 days, it may be reasonable to predict that such $FeSe_2/Bi_2Se_3$-PEG may be a relatively safe agent to mice at our tested dose.

3. Conclusions

In summary, $FeSe_2/Bi_2Se_3$ nanostructures are successfully synthesized via cation exchange in this work and used for multimodal imaging and synergistic tumor therapy. By carefully changing the amount of added Bi, the density of $FeSe_2$ nanoparticles decorated on the surface of the Bi_2Se_3 nanosheets could be tuned. After PEGylation, $FeSe_2/Bi_2Se_3$-PEG exhibits excellent compatibility in various physiological solutions. With a high r_2 relaxivity, strong X-ray and NIR absorbance, as well as the chelate-free radiolabeling by ^{64}Cu, such composite-nanostructure is able to offer contrasts in tetra-modal MR/CT/PA/PET imaging, which vividly illustrates efficient tumor homing of $FeSe_2/Bi_2Se_3$-PEG after *i.v.* injection. Again utilizing the intrinsic physical properties of $FeSe_2/Bi_2Se_3$-PEG, *in vivo* photothermal & radiation therapy with a remarkable synergistic tumor destruction effect is realized. The relatively rapid excretion with little retention after 30 days upon systemic administration, together with the observed no appreciable toxic side effect are also promising for their further in vivo applications. Therefore, our work presents a new class of two-dimensional composite-nanostructure with highly integrated functions interesting in cancer theranostics. Moreover, the general method developed in this work may be applied to the synthesis of other types of composite-nanostructures not only for applications in biomedicine, but also potentially useful in catalyst, energy storage, and other different fields.

Experimental section

Materials

All the chemical reagents, unless specified, were purchased and used without further purification. Iron (II) chloride tetrahydrate ($FeCl_2\cdot4H_2O$), Bismuth (III) nitrate pentahydrate ($Bi(NO_3)_3\cdot5H_2O$), Oleylamine (OM), 1-Ethyl-3-(3-dimethylaminopropyl) carbodiimide (EDC), triethylamine (TEA) and 1-octadecene (ODE) were purchased from Sigma-Aldrich. Diethylene glycol (DEG) and Senium powder (Se) were obtained from Sinopharm Chemical Reagent Co., Ltd. (China). Poly (maleic anhydride-alt-1-octadecene) (C18PMH) polymers were purchased from Sigma-Aldrich and mPEG-NH_2 (MW=5K) were obtained from

Biomatrik Co., Ltd (Jiaxing, China). Deionized water used in our experiments was obtained by using a Milli-Q water system.

Synthesis of FeSe$_2$/Bi$_2$Se$_3$ nanostructures

FeSe$_2$/Bi$_2$Se$_3$ nanostructures were prepared by a one-step cation exchange method. In brief, 15mL oleyl amine (OM) and 10 mL octadecene (ODE) were added to a three-necked flask (50 mL) at room temperature. The solution was heated to 120 °C under nitrogen protection and kept under this temperature for 30 min. Then 1 mmol FeCl$_2$·4H$_2$O was quickly added to the above solution followed by vigorous magnetic stirring for 30 min. Next, An Se/OM solution prepared by dissolving 2 mmol of Se powder in 4 ml of OM was slowly injected into the flask at 150 °C within 10 min. Then reaction was kept at 150 °C for another 30 min to generate FeSe$_2$ nanoparticles. After that, Bi/DEG solutions prepared by dissolving Bi (NO$_3$)$_3$·5H$_2$O in 4 ml of diethylene glycol (DEG) with different concentrations (0.2, 0.5, 1, 1.5 and 2 mmol) were then injected into the above flask at 150 °C within 10 min. The reaction was kept at 150 °C for another 30 min. After the reaction, the products were cooled to room temperature. To precipitate the generated FeSe$_2$/Bi$_2$Se$_3$ nanostructures, excess ethanol was added. FeSe$_2$/Bi$_2$Se$_3$ nanostructures were then collected by centrifugation at 14800 round-per-min (rpm) and washed repeatedly with hexane and ethanol. The final product was dispersed in ethanol and stored at 4°C for future use.

Functionalization of FeSe$_2$/Bi$_2$Se$_3$ nanostructures

C$_{18}$PMH-PEG was synthesized following a literature procedure[31]. 4 ml stock solution of FeSe$_2$/Bi$_2$Se$_3$ (5 mg/mL) was precipitated by centrifugation, washed twice with ethanol, and then dispersed in chloroform, into which another solution of 50 mg C$_{18}$PMH-PEG polymer in 2 ml chloroform was added. The mixture was stirred for 4 h. After blowing-dry chloroform, the residue was readily dissolved in water. The resultant solution was centrifuged at 14800 rpm to remove large aggregates and gotten FeSe$_2$/Bi$_2$Se$_3$-PEG solution.

Characterization

The phase and crystallography of the products were characterized by using a PANalytical X-ray diffractometer equipped with Cuka radiation (λ=0.15406 nm). A scanning rate of 0.05 °S^{-1} was applied to record the patterns in the 2θ range of 10–80°. Transmission electron microscopy (TEM) images of the nanostructures were obtained using a FEI Tecnai F20 transmission electron microscope. Atomic force microscopy (AFM) images were taken by MultiMode V atomic force microscopy (Veeco, USA). X-ray photoelectron spectra (XPS) was performed on an SSI S-Probe XPS Spectrometer. UV-vis-NIR spectra were obtained with PerkinElmer Lambda 750 UV-vis-NIR spectrophotometer. The dynamic diameter of FeSe$_2$/Bi$_2$Se$_3$-PEG solution was determined by a Zetasizer Nano-ZS (Malvern Instruments, UK). Concentrations of Fe and Bi were measured by inductively coupled plasma atomic emission spectroscopy (ICP-AES).

Cell culture experiments

4T1 murine breast cancer cells were cultured in the standard cell culture medium recommended by American type culture collection (ATCC) supplemented with 10% FBS

and 1% penicillin/streptomycin at 37°C in a 5% CO_2-containing atmosphere. Cells seeded into 96 well plates at a density of $1*10^4$ cells per well were incubated with different concentrations of $FeSe_2/B_{i2}Se_3$-PEG nanostructures for 24 h. Relative cell viabilities were determined by the standard 3-(4,5-dimethylthiazol-2-yl)-2,5-diphenyltetrazolium bromide (MTT) assay.

Tumor model

Balb/c mice were obtained from Nanjing Peng Sheng Biological Technology Co. Ltd. and used under protocols approved by Soochow University Laboratory Animal Center. The 4T1 tumors were generated by subcutaneous injection of $1*10^6$ cells in ~30 μL serum-free RMPI-1640 medium onto the back of each female Balb/c mice.

In vivo multimodal imaging

For T2-MR imaging, tumor-bearing mice were intravenously injected with $FeSe_2/Bi_2Se_3$-PEG (200μl, 2 mg/mL). T2-weighted MR images were taken on a 3T clinical MRI scanner (Bruker Biospin Corporation, Billerica, MA, USA) equipped with small animal imaging coil. T2-weighted images were acquired using the following parameters: TR 2000 ms; TE 106.4 ms; slice thickness 2.0 mm; slice spacing, 0.2 mm; matrix, 224×192; FOV 10 cm×10 cm.

For CT imaging, $FeSe_2/Bi_2Se_3$-PEG solutions of different concentrations ranging from 1 to 10 mg/mL were placed in 0.5 mL tubes. Images were obtained and data were analyzed by recording the Hounsfield units (HUs) for regions of interest (ROI). CT images were reconstructed with CT values calculated from raw data using 3D-Med software. For *in vivo* studies, the tumor-bearing mice were anesthetized by isoflurane. Then, 200 μL of $FeSe_2/Bi_2Se_3$-PEG solution (5 mg/mL) were *i.v.* injected. CT images were acquired before and 24 h after $FeSe_2/Bi_2Se_3$-PEG administration.

PA imaging was performed with a preclinical photoacoustic computed tomography scanner (Endra Nexus 128, Ann Arbor, MI). During our experiments, anesthesia was maintained using isoflurane. The body temperature of the mice was maintained by using a water heating system at 37.5°C. 4T1 tumor-bearing mice were *i.v.* injected with $FeSe_2/Bi_2Se_3$-PEG solution prior to imaging (2 mg/mL, 200 μL).

[64]Cu labeling and animal modal for PET imaging

[64]Cu was produced with an onsite cyclotron (GE PETtrace). $^{64}CuCl_2$ (150 MBq) was diluted in 300 μL of 0.1 M sodium acetate buffer (pH 5.5) and mixed with 30 μL of $FeSe_2/Bi_2Se_3$-PEG (1 mg/mL). The reaction was conducted at 37 °C for 60 min with constant shaking. The labeling yield was determined by thin-layer chromatography (TLC) at different time points. The resulting [64]Cu-$FeSe_2/Bi_2Se_3$-PEG was purified by a PD-10 column using PBS as the mobile phase.

Serum stability study was carried out to ensure ^{64}Cu is stably attached on $FeSe_2/Bi_2Se_3$-PEG for *in vivo* PET imaging. [64]Cu-$FeSe_2/Bi_2Se_3$-PEG was incubated in PBS and complete serum at 37 °C for up to 24 h. At different time points, portions of the mixture were sampled

and filtered through 100 kDa MWCO filters. The radioactivity that remained on the filter was measured after discarding the filtrate. The retained (i.e., intact) ^{64}Cu on $FeSe_2/Bi_2Se_3$-PEG was calculated using the equation (radioactivity on filter/total sampled radioactivity × 100%).

For PET imaging, 4T1 tumor-bearing mice (3 mice per group) post *i.v* injection of 5~10 MBq of ^{64}Cu-$FeSe_2/Bi_2Se_3$-PEG solution were performed using a microPET/microCT Inveon rodent model scanner (Siemens Medical Solutions USA, Inc.). Data acquisition, image reconstruction, and ROI analysis of the PET data were performed as described previously[32].

In vitro PTT—4T1 cancer cells at a density of $1*10^4$ cells per well were incubated with various concentrations of $FeSe_2/Bi_2Se_3$-PEG for 6 h and then irradiated by an 808-nm laser at the power density of 0.8 W/cm^2 for 5 min. The cells were stained with Calcein-AM and propidium iodide (PI) for 15 min, washed with PBS, and then imaged by a Confocal fluorescence microscope (Leica).

In vitro RT—For clonogenic assay, 4T1 cells were cultured in 6-well plate at a density of $1*10^3$ cells per well and incubated at 37 °C for 24 h. Then the cells were treated with $FeSe_2/Bi_2Se_3$-PEG (30 μg/mL). Untreated cells were used as the control. After 6 h of incubation, the cells were then received irradiation of X-ray with specified radiation doses (0, 2, 4, and 6 Gy). The cells were washed with PBS (pH=7.4) and further incubated at 37 °C for 10 days, before they were fixed with anhydrous ethanol and stained with Crystal violet (CV, Sigma-Aldrich). The resulting colonies were counted only if it contained more than 50 cells. The surviving fraction = (surviving colonies)/(cells seeded × plating efficiency). The mean surviving fraction was obtained from three parallel tests.

For γ-H2AX immunoflourescence analysis, 4T1 cells seeded in 12-well plate were incubated with $FeSe_2/Bi_2Se_3$-PEG (0 or 30 μg/mL) for 6 h, and then irradiated with X-ray at the dose of 4 Gy. After 2 h of incubation, the cells were fixed by 4 % of paraformaldehyde for 10 min and then rinsed in PBS (pH=7.4). Then the cells were permeabilized with methanol for 15 min at −20 °C and rinsed in PBS. The cells were exposed to a blocking buffer (1% BSA in PBS solution) for 1h at room temperature and subsequently further incubated with the primary antibody (mouse monoclonal anti-phospho-histone γ-H2AX, 1:500 in PBS containing 1% BSA) overnight at 4°C. After PBS washing, the cells were incubated with the secondary antibody (sheep anti-mouse Cy633, 1:500 in PBS containing 1% BSA) for 1 h at room temperature. Excess dye-labeled antibody was removed by rinsing the coverslips in PBS. Cell nuclei were stained by DAPI for 5 min at room temperature. The cells were imaged using a confocal fluorescence microscopy (Leica SP5).

In vivo RT&PTT combined therapy

To development the tumor model, 4T1 cells (1×10^6) suspended in 30 μL of PBS were subcutaneously injected into the back of each Balb/c mouse. After the tumor volume reached ~70 mm^3, mice were randomly divided into seven groups (n = 5 per group) for various treatment: Control (i), $FeSe_2/Bi_2Se_3$-PEG injected (ii), Laser only (iii), $FeSe_2/Bi_2Se_3$-PEG +Laser (iv), RT only (v), $FeSe_2/Bi_2Se_3$-PEG+RT (vi), and $FeSe_2/Bi_2Se_3$-PEG+ Laser + RT

(vii). $FeSe_2/Bi_2Se_3$-PEG at the dose of 20 mg/kg was *i.v.* injected into mice bearing 4T1 tumors. PTT or RT treatments were conducted 24 h later, with the 808-nm NIR laser (Hi-Tech Optoelectronics Co., Ltd. Beijing, China) at the power density of 0.5 W/cm^2 for 10 min, or the X-ray irradiation at the dose of 4 Gy, respectively. The tumor surface temperatures were recorded by an IR thermal camera (IRS E50 Pro Thermal Imaging Camera). The tumor sizes were measured by a caliper every the other day and calculated as the volume = (tumor length) $\times$ (tumor width)^2/2. Relative tumor volumes were calculated as V/V_0 (V_0 was the initial tumor volume). Two days after treatment, the tumors in group (i), (iv), (vi), and (vii) were dissected to make paraffin sections for further hematoxylin and eosin (H&E) staining.

In vivo toxicity

Healthy Balb/c mice were *i.v.* injected with $FeSe_2/Bi_2Se_3$-PEG (200 μL, 20 mg/kg) and sacrificed at various time points (1 day, 7 days, 14 days, and 30 days p.i., five mice per time point) after injection. Another five healthy Balb/c mice were used as the control. Before the mice were euthanized, blood samples (~ 1 mL) were collected and sent to Shanghai Research Center of Biomodel Organism for blood panel analysis and blood chemistry test. Major organs of those mice were harvested and divided into two halves for biodistribution measurement and histological examination, respectively. For biodistribution measurement, major organs, including liver, spleen, kidney, heart, lung, stomach, intestine, skin, muscle and bone, from mice treated with and without $FeSe_2/Bi_2Se_3$-PEG solution were solubilized by aqua regia for ICP-AES measurement to determine bismuth levels in various organs. For histological examination, organs from the treated groups and the control group were fixed in 4% formalin and then conducted with paraffin embedded sections for H&E staining. The slices were examined and observed by a digital microscope (Leica QWin).

Supplementary Material

Refer to Web version on PubMed Central for supplementary material.

Acknowledgments

References

1. a Bardhan R, Lal S, Joshi A, Halas NJ. Acc Chem Res. 2011; 44:936. [PubMed: 21612199] b Yoo D, Lee JH, Shin TH, Cheon J. Acc Chem Res. 2011; 44:863. [PubMed: 21823593] c Xia Y, Li W, Cobley CM, Chen J, Xia X, Zhang Q, Yang M, Cho EC, Brown PK. Acc Chem Res. 2011; 44:914. [PubMed: 21528889] d Cheng L, Wang C, Feng L, Yang K, Liu Z. Chem Rev. 2014; 114:10869. [PubMed: 25260098]

2. a Pysz MA, Gambhir SS, Willmann JK. Clin Radiol. 2010; 65:500. [PubMed: 20541650] b Lee DE, Koo H, Sun IC, Ryu JH, Kim K, Kwon IC. Chem Soc Rev. 2012; 41:2656. [PubMed: 22189429] c Xie J, Liu G, Eden HS, Ai H, Chen X. Acc Chem Res. 2011; 44:883. [PubMed: 21548618]

3. a Kumar CS, Mohammad F. Adv Drug Delivery Rev. 2011; 63:789.b Della Rocca J, Liu D, Lin W. Acc Chemical Res. 2011; 44:957.c Liu Z, Chen K, Davis C, Sherlock S, Cao Q, Chen X, Dai H. Cancer Res. 2008; 68:6652–6660. [PubMed: 18701489] d Cheng L, Yang K, Li Y, Chen J, Wang C, Shao M, Lee ST, Liu Z. Angew Chem, Int Ed. 2011; 123:7523.e Chen Q, Ke H, Dai Z, Liu Z. Biomaterials. 2015; 73:214. [PubMed: 26410788] f Zhang Y, Jeon M, Rich LJ, Hong H, Geng J, Zhang Y, Shi S, Barnhart TE, Alexandridis P, Huizinga JD, Seshadri M, Cai W, Kim C, Lovell JF. Nat Nanothechnol. 2014; 9:631.g Kaaki K, Hervé-Aubert K, Chiper M, Shkilnyy A, Soucé M, Benoit R, Paillard A, Dubois P, Saboungi ML, Chourpa I. Langmuir. 2012; 28:1496. [PubMed: 22172203]

4. a Hainfeld JF, Slatkin DN, Smilowitz HM. Phys Med Biol. 2004; 49:309.b Chithrani DB, Jelveh S, Jalali F, Prooijen Mv, Allen C, Bristow RG, Hill RP, Jaffray DA. Radiat Res. 2010; 173:719. [PubMed: 20518651]

5. Ma M, Huang Y, Chen H, Jia X, Wang S, Wang Z, Shi J. Biomaterials. 2015; 37:447. [PubMed: 25453972]

6. Gai S, Li C, Yang P, Lin J. Chem Rev. 2013; 114:2343. [PubMed: 24344724]

7. a Lord CJ, Ashworth A. Nature. 2012; 481:287–294. [PubMed: 22258607] b Wilson WR, Hay MP. Nat Rev Cancer. 2011; 11:393. [PubMed: 21606941]

8. a Robinson JT, Tabakman SM, Liang Y, Wang H, Sanchez Casalongue H, Vinh D, Dai H. J Am Chem Soc. 2011; 133:6825. [PubMed: 21476500] b Yang K, Feng L, Shi X, Liu Z. Chem Soc Rev. 2013; 42:530. [PubMed: 23059655] c Huang X, El-Sayed IH, Qian W, El-Sayed MA. J Am Chem Soc. 2006; 128:2115. [PubMed: 16464114] d Huang X, Tang S, Mu X, Dai Y, Chen G, Zhou Z, Ruan F, Yang Z, Zheng N. Nat Nanotechnol. 2011; 6:28. [PubMed: 21131956] e Tian Q, Hu J, Zhu Y, Zou R, Chen Z, Yang S, Li R, Su Q, Han Y, Liu X. J Am Chem Soc. 2013; 135:8571. [PubMed: 23687972] f Ke H, Wang J, Dai Z, Jin Y, Qu E, Xing Z, Guo C, Yue X, Liu J. Angew Chem, Int Ed. 2011; 50:3017.g Cheng L, Yang K, Chen Q, Liu Z. ACS Nano. 2012; 6:5605. [PubMed: 22616847] h Chen Z, Wang Q, Wang H, Zhang L, Song G, Song L, Hu J, Wang H, Liu J, Zhu M, Zhao D. Adv Mater. 2013; 25:2095. [PubMed: 23427112] i Cheng L, Liu J, Gu X, Gong H, Shi X, Liu T, Wang C, Wang X, Liu G, Xing H. Adv Mater. 2014; 26:1886. [PubMed: 24375758] j Wang QH, Kalantar-Zadeh K, Kis A, Coleman JN, Strano MS. Nat Nanotechnol. 2012; 7:699. [PubMed: 23132225]

9. Song G, Liang C, Gong H, Li M, Zheng X, Cheng L, Yang K, Jiang X, Liu Z. Adv Mater. 2015; 27:6110. [PubMed: 26331476]

10. a Xie J, Lee S, Chen X. Adv Drug Delivery Rev. 2010; 62:1064.b Tan C, Zhang H. Chem Soc Rev. 2015; 44:2713. [PubMed: 25292209]

11. Wang S, Li X, Chen Y, Cai X, Yao H, Gao W, Zheng Y, An X, Shi J, Chen H. Adv Mater. 2015; 27:2775. [PubMed: 25821185]

12. a Zhang XD, Chen J, Min Y, Park GB, Shen X, Song SS, Sun YM, Wang H, Long W, Xie J. Adv Funct Mater. 2014; 24:1718.b Liu J, Zheng X, Yan L, Zhou L, Tian G, Yin W, Wang L, Liu Y, Hu Z, Gu Z, Chen C, Zhao Y. ACS Nano. 2015; 9:696. [PubMed: 25561009]

13. a Luo YR. CRC Handbook of Chemistry and Physics. 2012; 88b) Schumann H, Arif AM, Rheingold AL, Janiak C, Hoffmann R, Kuhn N. Inorg Chem. 1991; 30:1618.

14. a Beberwyck BJ, Alivisatos AP. J Am Chem Soc. 2012; 134:19977. [PubMed: 23190283] b Son DH, Hughes SM, Yin Y, Alivisatos AP. Science. 2004; 306:1009. [PubMed: 15528440]

15. Yang K, Zhang S, Zhang G, Sun X, Lee ST, Liu Z. Nano Lett. 2010; 10:3318. [PubMed: 20684528]

16. Chou SS, Kaehr B, Kim J, Foley BM, De M, Hopkins PE, Huang J, Brinker CJ, Dravid VP. Angew Chem, Int Ed. 2013; 125:4254.

17. Wang J, Duan H, Lin X, Aguilar V, Mosqueda A, Zhao G-m. J Appl Phys. 2012; 112:103905. [PubMed: 23258940]

18. a Wang YXJ. Quant Imaging Med Surg. 2011; 1:35. [PubMed: 23256052] b Jung CW, Jacobs P. Magnetic Resonance Imaging. 1995; 13:661–674. [PubMed: 8569441] c Jung CW. Magn Reson Imaging. 1995; 13:675. [PubMed: 8569442]

19. a Li J, Jiang F, Yang B, Song XR, Liu Y, Yang HH, Cao DR, Shi WR, Chen GN. Sci Rep. 2013; 3:1998. [PubMed: 23770650] b Lusic H, Grinstaff MW. Chem Rev. 2013; 113:1641. [PubMed: 23210836] c Li B, Ye K, Zhang Y, Qin J, Zou R, Xu K, Huang X, Xiao Z, Zhang W, Lu X, Hu J. Adv Mater. 2015; 27:1339. [PubMed: 25639509]

20. Kim J, Piao Y, Hyeon T. Chem Soc Rev. 2009; 38:372. [PubMed: 19169455]

21. Nahrendorf M, Zhang H, Hembrador S, Panizzi P, Sosnovik DE, Aikawa E, Libby P, Swirski FK, Weissleder R. Circulation. 2008; 117:379. [PubMed: 18158358]

22. a Yang JM, Favazza C, Chen R, Yao J, Cai X, Maslov K, Zhou Q, Shung KK, Wang LV. Nat Med. 2012; 18:1297. [PubMed: 22797808] b De La Zerda A, Zavaleta C, Keren S, Vaithilingam S, Bodapati S, Liu Z, Levi J, Smith BR, Ma TJ, Oralkan O. Nat Nanotechnol. 2008; 3:557. [PubMed: 18772918]

23. a Sun X, Cai W, Chen X. Acc Chem Res. 2015; 48:286. [PubMed: 25635467] b Cai W, Chen X. J Nucl Med. 2008; 49:113S. [PubMed: 18523069]

24. Chen F, Hong H, Zhang Y, Valdovinos HF, Shi S, Kwon GS, Theuer CP, Barnhart TE, Cai W. ACS Nano. 2013; 7:9027. [PubMed: 24083623]

25. Zhou M, Zhang R, Huang M, Lu W, Song S, Melancon MP, Tian M, Liang D, Li C. J Am Chem Soc. 2010; 132:15351. [PubMed: 20942456]

26. a Liu T, Shi S, Liang C, Shen S, Cheng L, Wang C, Song X, Goel S, Barnhart TE, Cai W. ACS Nano. 2015; 9:950. [PubMed: 25562533] b Lee YJ, Seo D, Kwon JY, Son G, Park MS, Choi YH, Soh JH, Lee HN, Lee KD, Yoon J. Tetrahedron. 2006; 62:12340.

27. Firsanov DV, Solovjeva LV, Svetlova MP. Clin Epigenet. 2011; 2:283.

28. Su XY, Liu PD, Wu H, Gu N. Cancer Biol Med. 2014; 11:86. [PubMed: 25009750]

29. a Song CW, Park H, Griffin RJ. Radiat Res. 2001; 155:515. [PubMed: 11260653] b Moeller BJ, Richardson RA, Dewhirst MW. Cancer Metastasis Rev. 2007; 26:241. [PubMed: 17440683]

30. Soo Choi H, Liu W, Misra P, Tanaka E, Zimmer JP, Itty Ipe B, Bawendi MG, Frangioni JV. Nat Biotechnol. 2007; 25:1165. [PubMed: 17891134]

31. Cheng L, He W, Gong H, Wang C, Chen Q, Cheng Z, Liu Z. Adv Funct Mater. 2013; 23:5893.

32. Cai W, Chen X. Nat Protoc. 2008; 3:89. [PubMed: 18193025]
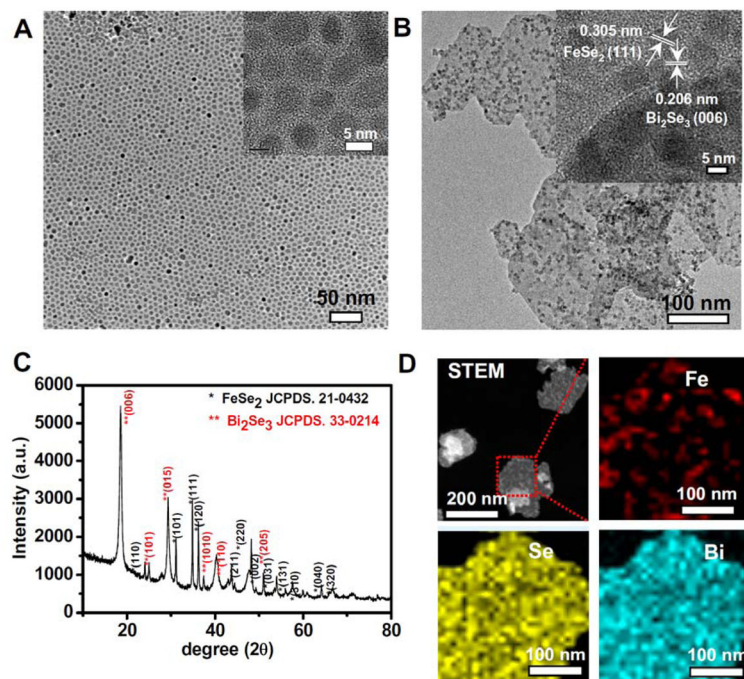
Figure 1.
Characterization of FeSe$_2$/Bi$_2$Se$_3$ nanostructures. (**A&B**) TEM images of FeSe$_2$ nanoparticles (**A**) and FeSe$_2$/Bi$_2$Se$_3$ nanostructures (prepared at 1 : 1 Bi : Fe feeding ratio, with 0.5 h of reaction time). Insets: the respective high-resolution TEM (HRTEM) images. (**C**) Powder XRD pattern of FeSe$_2$/Bi$_2$Se$_3$ nanostructures. (**D**) HAADF-STEM-EDS images of FeSe$_2$/Bi$_2$Se$_3$ nanostructures. The element maps showed the distribution of Fe (red), Se (yellow), and Bi (Cyan).
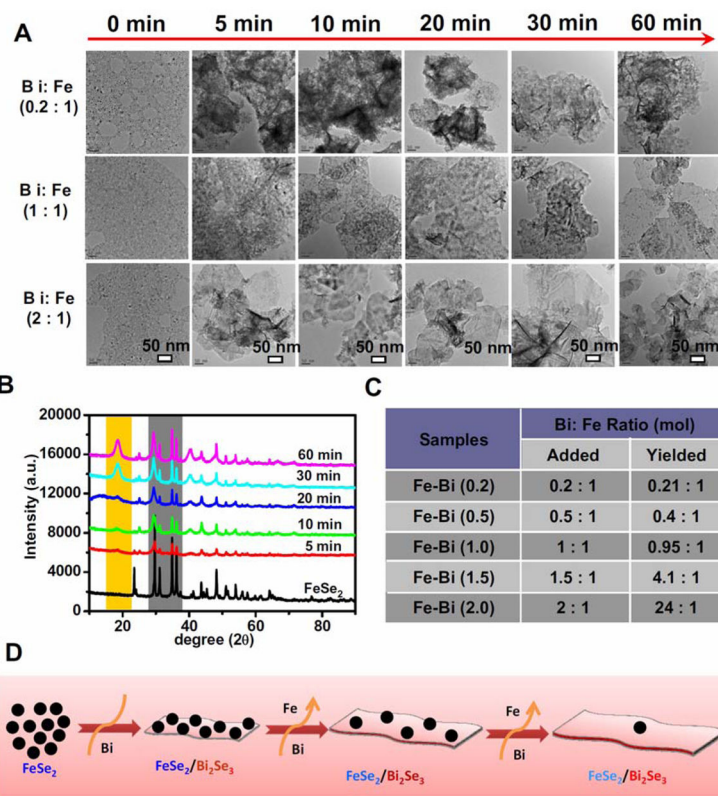
Figure 2.

Synthesis of $FeSe_2/Bi_2Se_3$ composite-nanostructures. (**A**) TEM images of $FeSe_2/Bi_2Se_3$ nanostructures prepared at different reaction time (5 min, 10 min, 20 min, 30 min, and 60 min) with various Bi : Fe feeding ratios from $FeSe_2$ nanoparticles. (**B**) Powder XRD spectra of $FeSe_2/Bi_2Se_3$ nanostructures (Bi: Fe ratio = 1 : 1) prepared by different reaction time (5 min, 10 min, 20 min, 30 min, and 60 min). (**C**) A table showing element compositions of the various $FeSe_2/Bi_2Se_3$ nanostructures with the various ratios of added Bi : Fe as determined by ICP-AES (reaction time = 30 min). (**D**) A scheme showing the mechanism of the synthesis of $FeSe_2/Bi_2Se_3$ nanostructures via cation exchange.
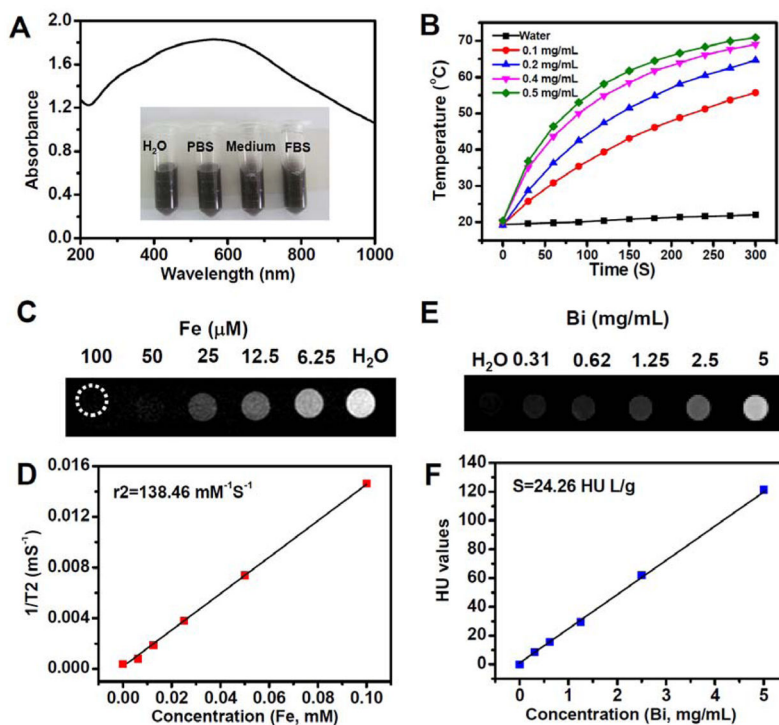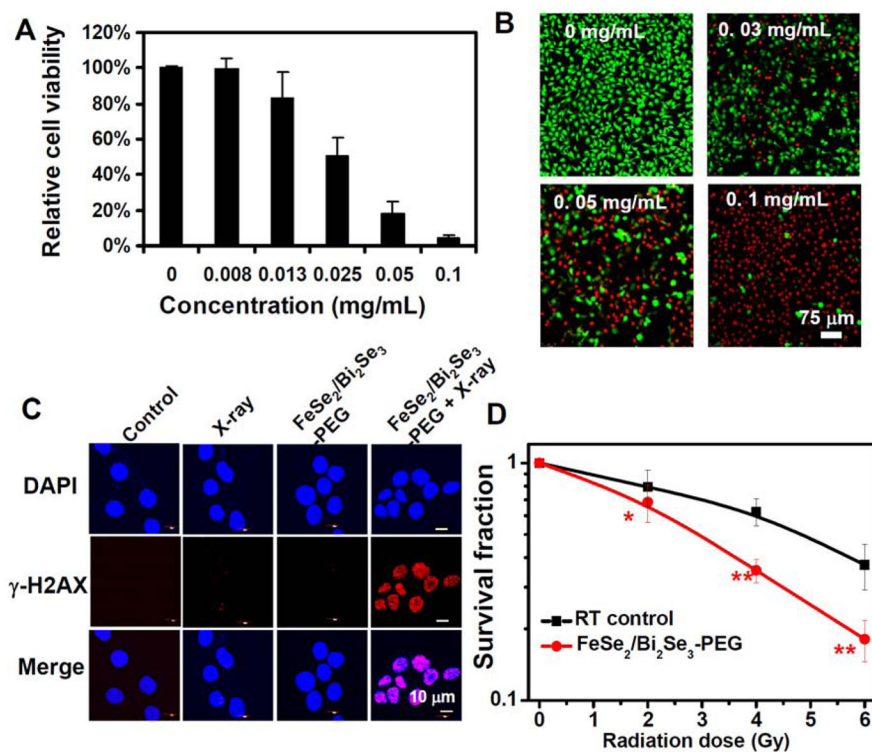
Figure 3.

Characterization of PEGylated $FeSe_2/Bi_2Se_3$ nanostructures. (**A**) UV-vis-NIR absorbance spectra of $FeSe_2/Bi_2Se_3$-PEG in water (0.1 mg/mL). (**B**) The photothermal heating curves of $FeSe_2/Bi_2Se_3$-PEG with different concentrations under 808-nm laser irradiation at the power density of 0.8 W/cm^2. (**C&D**) T2 weighted MR images (**C**) and T2 relaxation rates (**D**) of $FeSe_2/Bi_2Se_3$-PEG solutions with different concentrations. (**E&F**) CT images (**E**) and HU values (**F**) of $FeSe_2/Bi_2Se_3$-PEG solutions with different concentrations.
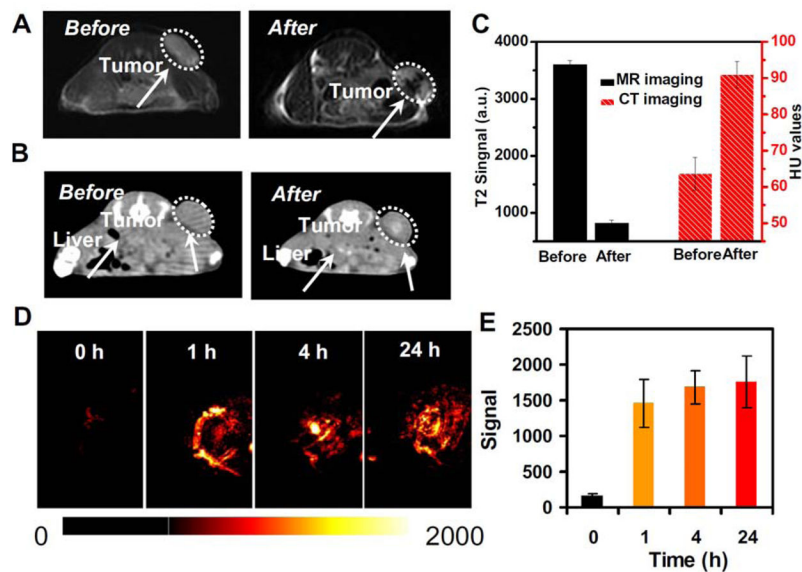
Figure 4.

In vivo tetra-modal imaging. (**A**) T2-weighted MR images of mice before and 24 h after i.v. injection with $FeSe_2/Bi_2Se_3$-PEG. (**B**) *In vivo* CT images of mice before and 24 h after i.v. injection with $FeSe_2/Bi_2Se_3$-PEG. (**C**) Quantified MR and CT signals of tumors from mice before and 24 h after i.v. injection of $FeSe_2/Bi_2Se_3$-PEG based on the above imaging data. (**D**) *In vivo* PA images of tumors on mice after injection with $FeSe_2/Bi_2Se_3$-PEG taken at different time points (0 h, 1 h, 4 h, and 24 h). (**E**) Quantified PA signals of tumors from mice after i.v. injection of $FeSe_2/Bi_2Se_3$-PEG.
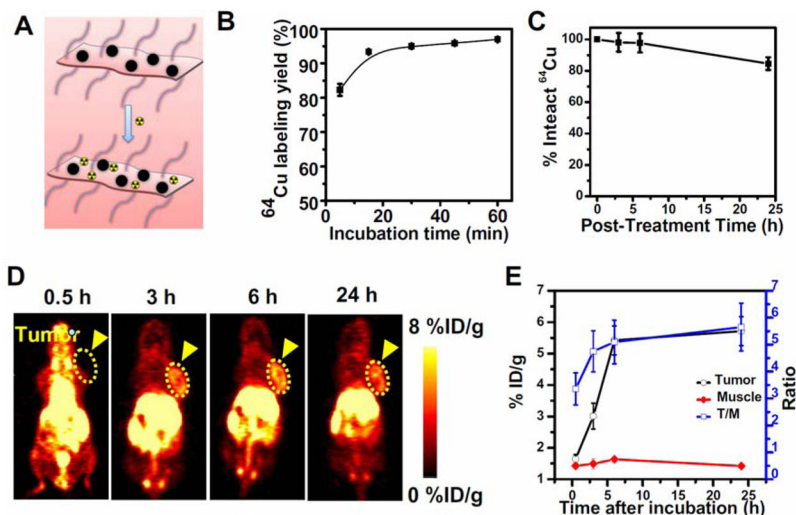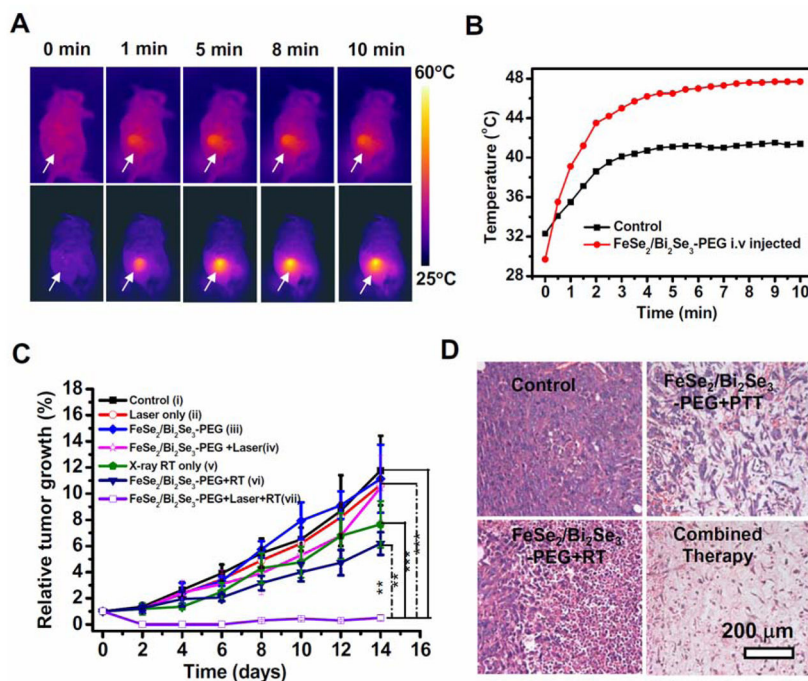
Figure 5.

^{64}Cu labeling on FeSe$_2$/Bi$_2$Se$_3$-PEG for PET imaging. (**A**) A scheme presenting ^{64}Cu labeling on FeSe$_2$/Bi$_2$Se$_3$-PEG via a chelator-free manner. (**B**) Quantified labeling yield of ^{64}Cu on FeSe$_2$/Bi$_2$Se$_3$-PEG at various time points after mixing (n = 3). (**C**). Stability test of ^{64}Cu labeling on FeSe$_2$/Bi$_2$Se$_3$-PEG after incubation in serum for different periods of time. (**D**) PET images of 4T1 tumor-bearing mice taken at various time points (0, 3 h, 6 h, and 24 h) post *i.v.* injection of ^{64}Cu-FeSe$_2$/Bi$_2$Se$_3$-PEG. (**E**) Quantification of ^{64}Cu-FeSe$_2$/Bi$_2$Se$_3$-PEG uptake in the tumor and muscle, as well as the tumor/muscle (T/M) ratios at various time points p.i. The unit is the percentage of injected dose per gram of tissue (%ID/g).
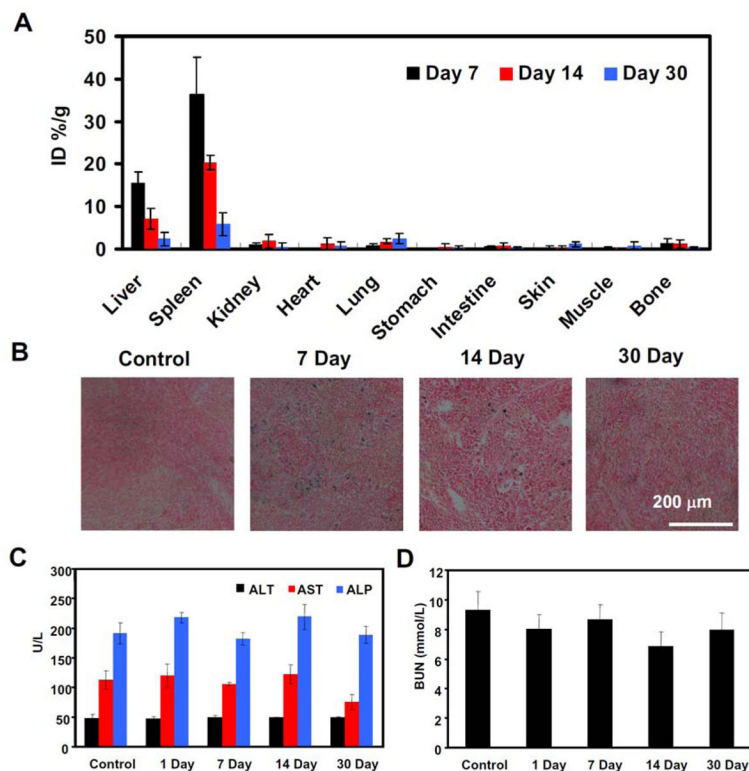
Figure 6.

In vitro photothermal therapy and radiation therapy. (**A**) Relative viabilities of 4T1 cells after $FeSe_2/Bi_2Se_3$-PEG-induced photothermal ablation at different nanoparticle concentrations. Error bars were based on the standard deviations (SD) of six parallel samples. (**B**) Confocal images of calcein AM (green, live cells) and propidium iodide (red, dead cells) co-stained cells after incubation with different concentration of $FeSe_2/Bi_2Se_3$-PEG and being exposed to the 808-nm laser at the power density of 0.8 W/cm^2 for 5 min. (**C**) Confocal fluorescence images of γ-H2AX stained 4T1 cells treated with PBS control, RT alone (4 Gy), $FeSe_2/Bi_2Se_3$-PEG, and $FeSe_2/Bi_2Se_3$-PEG + RT (4 Gy). (**D**) Clonogenic survival assay of 4T1 cells treated with or without $FeSe_2/Bi_2Se_3$-PEG under a series of radiation doses at 0, 2, 4, and 6 Gy. Error bars represent SD of at least three replicates. P values: *$P < 0.05$, **$P < 0.01$.

Figure 7.

In vivo combined photothermal & radiation therapy. (**A**) IR thermal images of 4T1 tumor-bear mice without (upper row) or with *i.v.* injection of FeSe$_2$/Bi$_2$Se$_3$-PEG (lower row, dose = 20 mg/kg, irradiated at 24 h p.i.), under the 808-nm laser irradiation taken at different time intervals. The laser power density was 0.5 W/cm^2. (**B**) Temperature changes of tumors monitored by the IR thermal camera during laser irradiation. (**C**) The tumor volume growth curves of mice after various treatments (5 mice for each group). Group i: Untreated control; Group ii: NIR laser only; Group iii: FeSe$_2$/Bi$_2$Se$_3$-PEG; Group iv: FeSe$_2$/Bi$_2$Se$_3$-PEG + NIR; Group v: X-ray RT alone; Group vi: FeSe$_2$/Bi$_2$Se$_3$-PEG + RT; Group vii: FeSe$_2$/Bi$_2$Se$_3$-PEG +NIR + RT. PTT was conducted by the 808-nm at 0.5 W/cm^2 for 10 min, while the irradiation dose of RT was 4 Gy. Error bars were based on standard error of the mean (SEM). (**D**) Micrographs of H&E stained tumor slices from different groups of mice treated with PBS, FeSe$_2$/Bi$_2$Se$_3$-PEG+NIR, FeSe$_2$/Bi$_2$Se$_3$-PEG+RT, and FeSe$_2$/Bi$_2$Se$_3$-PEG+RT +NIR. The tumors were harvested 2 days after treatments were conducted.

Figure 8.

Biodistribution and *in vivo* long-term toxicity data. (**A**) Biodistribution of Bi in major organs after various periods of time (7, 14, and 30 days) post *i.v.* injection with $FeSe_2/Bi_2Se_3$-PEG as measured by ICP-AES (dose=20 mg/kg, n=5). (**B**) Representation Prussian blue stained images of spleen collected from untreated control mice and $FeSe_2/Bi_2Se_3$-PEG (20 mg/kg) injected mice at different time points post-injection. (**C–D**) Blood biochemistry and hematology data of female Balb/c mice treated with $FeSe_2/Bi_2Se_3$-PEG at the dose of 20 mg/kg at 1 day, 7 days, 14 days, and 30 days p.i. Five mice without injection were used as the un-treated control. (**C**) ALT, ALP and AST levels in the blood at various time points after $FeSe_2/Bi_2Se_3$-PEG treatment. (**D**) Blood urea nitrogen (BUN) over time.
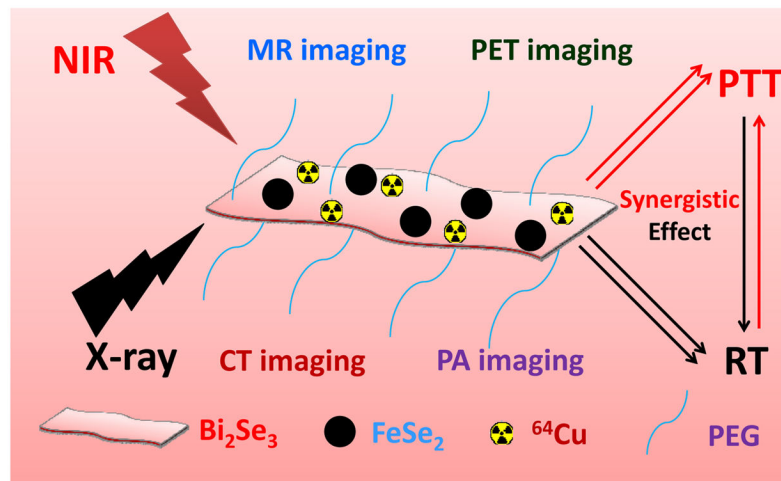
Scheme 1.
A scheme showing the structure of $FeSe_2/Bi_2Se_3$ composite-nanostructure for multimodal imaging and photothermal-radiation combined tumor therapy.